

How ice shelf morphology controls basal melting

Christopher M. Little

Princeton University, Department of Geosciences

Anand Gnanadesikan

NOAA/Geophysical Fluid Dynamics Laboratory, Princeton NJ

Michael Oppenheimer

Department of Geosciences and Woodrow Wilson School of Public and International
Affairs, Princeton University, Princeton NJ

Received:

*Corresponding author address:

Christopher M. Little
Room 28, Guyot Hall
Department of Geosciences
Princeton University
Princeton NJ 08544

cmlittle@princeton.edu

1 **ABSTRACT**

2 The response of ice shelf basal melting to climate is a function of ocean temperature,
3 circulation, and mixing outside the ice shelf cavity -- and the coupling of this external
4 forcing to the sub-ice shelf circulation. Because slope strongly influences the properties
5 of buoyancy-driven flow near the ice shelf base, ice shelf morphology plays a critical role
6 in linking external, subsurface heat sources to the ice. In this paper, the slope-driven
7 dynamic control of local and area-integrated melting rates is examined under conditions
8 similar to those in the Amundsen Sea, where small, steep ice shelves are exposed to
9 warm subsurface waters. A 3-D numerical ocean model is used to simulate the circulation
10 underneath five idealized ice shelves, forced with subsurface ocean temperatures ranging
11 from -2.0°C to 1.5°C. In the sub-ice shelf mixed layer, three spatially distinct dynamic
12 regimes are present. Entrainment of heat occurs predominately under deeper sections of
13 the ice shelf; local and area-integrated melting rates are most sensitive to changes in slope
14 in this *initiation* region. Some entrained heat is advected upslope and used to melt ice in
15 the *maintenance* region; however, flow convergence in the *outflow* region limits heat loss
16 in flatter portions of the ice shelf. Heat flux to the ice exhibits: 1) a spatially non-uniform,
17 super-linear dependence on slope and 2) a shape and temperature-dependent, internally-
18 controlled, efficiency. Because the efficiency of heat flux through the mixed layer
19 decreases with ocean temperature, numerical simulations diverge from a simple quadratic
20 scaling law.

INTRODUCTION

Basal melting of Antarctic ice shelves influences ice sheet dynamics [Dupont and Alley, 2005, 2006; Payne, et al., 2004; Schoof, 2007]; the meltwater produced freshens and cools the circumpolar ocean [Hohmann, et al., 2002; Jacobs, et al., 1996; Orsi, et al., 1999]. Ocean-driven changes in melting rates or locations thus influence watermass properties, climate, and sea level. Yet the linkage between ocean heat fluxes, basal melting, and ice discharge is blurred by physical uncertainties, observational limitations, and finite computing resources [Little, et al., 2007]. The lack of clarity is particularly tangible in the Amundsen Sea sector of Antarctica, where increases in basal melting have triggered rapid ice shelf thinning [Shepherd, et al., 2004] and grounded ice loss [Payne, et al., 2004; Rignot, 2008]. Although upwelling near the continental shelf break may have initiated this process [Thoma, et al., 2008], the mechanisms linking on-shelf heat fluxes to basal melting have not been conclusively demonstrated.

The complex, coupled nature of ice sheet-ocean interaction has inspired a search for key parameters governing the melting rate. Observations, simplified equation sets, and numerical models have been used to formulate scaling laws in which sub-ice shelf ocean temperature is related to area-averaged melt rates [Holland, et al., 2008 (HJH08); MacAyeal, 1984; Rignot and Jacobs, 2002]. Despite growing support for a super-linear temperature-dependence, these studies exhibit divergence [HJH08, figure 1], implying that some physical processes are missing. It remains unclear whether prior results are valid across different ice shelves and a large range of temperatures. Observationally-derived scaling laws [Rignot and Jacobs, 2002] aggregate ice shelves with widely varying morphologies; temperature and shape-dependence may be conflated. Even if an

ocean temperature-based scaling is robust across ice shelves, area-integrated melt rates overlook the spatial variability of melting (as well as any glaciological response). Recent modeling and theoretical studies indicate that the distribution, rather than the total amount, of basal melting is critical to ice flow [*Schoof, 2007; Walker, et al., 2008*].

Here we investigate an additional control on the distribution and area-integrated rate of ocean-driven melting: the basal slope of the ice shelf. In boundary-trapped, buoyancy-driven oceanic flow, local slope drives the Richardson number down, and thus increases entrainment (mixing across stratified layers) [*Ellison and Turner, 1959; Jenkins, 1991; Pedersen, 1980*]. Since meltwater-freshened layers near the ice shelf base are relatively cold and stable [*Nicholls, et al., 2006; Nicholls, et al., 2001*], enhanced entrainment in regions of steeper basal slope might be expected to lead to relatively high melting rates.

Observations and models of ice shelves support the importance of basal slope. Patterns of basal melting are highly non-uniform [*Joughin and Padman, 2003*], and there is evidence [*Payne, et al., 2007; Rignot and Steffen, 2008*] that enhanced melting near (steep) grounding lines is characteristic of small ice shelves. Even under uniform forcing, models employing realistic ice shelf thickness gradients simulate an intensified longitudinal gradient in melting [*HJH08*]. In coupled ice-ocean models, ice shelf thickness gradients co-evolve with intensified melting near grounding lines [*Grosfeld and Sandhager, 2004; Walker and Holland, 2007*].

The physical processes underlying the sensitivity of basal melting rates to ice shelf morphology, either in isolation or in conjunction with thermal forcing, have not been formally assessed. Here, we find that slope-dependent turbulent mixing drives high

67 mixed layer temperatures in steep regions; the rate of ice-ocean heat transfer and the
68 mixed layer thickness control where entrained heat is used for melting. The relative
69 magnitude of the entrainment rate and the ice-ocean thermal exchange velocity governs
70 the local response to changes in slope. The distribution of melting, area-integrated
71 melting rates, and the response to changes in ocean heat content and basal slope thus
72 depend on ice shelf morphology. The models employed here assume an infinite heat
73 reservoir; scenarios where heat is limited by open-ocean dynamics are not considered.
74 Although interaction with external processes adds complexity to this analysis, the
75 glaciological control of near-ice ocean properties is likely to remain important.

76 This paper is organized as follows: in the introduction, the key barriers to heat
77 flux and details of the numerical model are reviewed; the results section describes the
78 mixed layer dynamic regimes and their influence on basal melting's sensitivity to
79 temperature and shape; the discussion highlights the physics underlying the results,
80 assesses the implications for glaciological and climate models, and underscores the
81 importance of the coupled ice-ocean response.

83 **SETTING UP THE PHYSICS**

84 *The efficiency of basal melting*

85 Only a fraction of the heat content of subsurface water is used to melt ice shelves;
86 here, this fraction is termed the efficiency of basal melting. As water is advected across
87 the continental shelf and under the ice shelf, efficiency losses can be quantified at
88 dynamic barriers. These barriers are illustrated schematically in figure 1; they include: 1)
89 the open-ocean mixed layer, where heat may be lost to the atmosphere; 2) the ice shelf

front, where a fraction of the subsurface water is advected under the ice shelf; 3) the sub-ice shelf mixed layer, where a fraction of interior water is entrained; 4) the ice-ocean interface, where mixed layer heat may be used to melt ice. Not all of the heat transferred to the ice shelf is used for melting; there may be significant conductive heat losses. This paper principally examines the efficiency of heat flux through the mixed layer, however, each barrier may influence the sensitivity of melting to open-ocean heat content.

The sub-ice mixed layer heat balance: Two barriers to melting

Insight into ice shelf-ocean heat fluxes can be gained from reduced-gravity models (i.e. with one active oceanic layer) of varying degrees of complexity [Jenkins, 1991; Payne, et al., 2007]. Several dynamical processes are absent from these models, including steady flow at depth [Little, et al., 2008] and time-dependent oceanic forcing [Makinson, 2002; Thoma, et al., 2008]. Yet a reduced-gravity approach is plausible for ice shelves exposed to a sluggish, relatively uniform, water mass; it is also a useful introduction to the dynamics further explored with 3-D numerical simulations.

In this framework, a well-mixed layer (schematically illustrated in figure 2) is comprised of interior water and meltwater. The mixed layer varies temporally and horizontally in depth, thermodynamic properties, and tracers, but is vertically homogeneous in tracers and momentum. The layer is lighter and cooler than the interior; its temperature (T) depends on the heat balance. In a steady state,

$$q_A = q_E + q_L + q_C \quad (1)$$

The heat fluxes in (1) refer to advection within the mixed layer (q_A), entrainment from the motionless interior (q_E), latent cooling (q_L), and conduction into the ice shelf (q_C).

Because the emphasis of this paper is on the oceanic heat balance, heat used to melt ice is defined to be negative (opposite to Q_M^T , as defined in Holland and Jenkins [1999]), and ice-ocean fluxes are aggregated, i.e. $q_I = q_L + q_C$.

Heat flux to the ice through a viscous sublayer may be modeled using an thermal exchange velocity, γ_T [Kader and Yaglom, 1972, 1977], such that:

$$q_I = \rho_0 c_p \gamma_T \Delta T_I \quad (2)$$

In (2), $\Delta T_I = T_B - T$ is the temperature difference across the sublayer, i.e. between the salinity and pressure-dependent freezing point and the local mixed layer temperature, c_p is the specific heat of the mixed layer, and ρ_0 is a oceanic reference density. Various formulations for the thermal exchange velocity have been proposed, incorporating stabilizing buoyancy fluxes and molecular diffusion, yet under most conditions, γ_T remains a strong function of the friction velocity, u^* [Holland and Jenkins, 1999]. Observational constraints on γ_T have been gained from a limited set of measurements under sea ice [McPhee, 1992, 1999].

Sublayer salt fluxes may be addressed with an analogous salinity exchange velocity (γ_S) [Mellor et al., 1986]. Slow diffusion of salt through the sublayer will increase the freezing point at the ice interface relative to that of the mixed layer. For simplicity, in this section, the mixed layer-ice temperature gradient is assumed to be large relative to salinity- or pressure-dependent changes in the freezing point. Variability in the freezing point is included in the numerical simulations.

Ignoring conduction and assuming a fully turbulent sublayer, the ice shelf melting rate is given by:

$$m' = -\frac{\rho_0}{\rho_i} \frac{c_p \gamma_T}{L_f} \Delta T_I \quad (3)$$

where ρ_I is the density of the ice shelf and L_f is the latent heat of fusion of ice. Mixed layer temperature (via ΔT_I) and flow speed (via γ_T) influence the melt rate. A positive melt rate indicates freshwater input to the mixed layer, driven by a mixed layer temperature above the in-situ freezing point.

Turbulent entrainment (e') across the base of the mixed layer supplies heat and salt to the mixed layer. Local shear is of primary importance, but entrainment is also influenced by stratification and non-local mixing processes. In the Amundsen, high melting rates and relatively weak tidal forcing [Padman, 2002] indicate that shear-driven entrainment, driven by buoyant, near-ice flow, is likely to be the dominant source of mixing. To date, ice shelf-ocean models have employed an interfacial Richardson number criterion [Holland and Feltham, 2005], or a surface-stress driven turbulent kinetic energy balance [Holland and Jenkins, 2001; Little, et al., 2008] to determine the rate of entrainment. (1) can then be expanded:

$$\mathbf{u} \bullet \nabla(hT) = -e' \Delta T_M + \gamma_T \Delta T_I \quad (4)$$

where $\Delta T_M = T - T_D$ is the temperature difference across the base of the mixed layer, T_D is the temperature of the interior, \mathbf{u} is the horizontal velocity, and h is the thickness of the mixed layer.

Further insight into the barriers to melting can be gained by assuming that advection is negligible. In this case, a 1-D local balance holds and (4) can be rewritten:

$$\frac{e'}{\gamma_T} = \frac{\Delta T_I}{\Delta T_M} \quad (5)$$

The ice shelf does not feel the unmodified interior temperature (T_D); heat is partitioned between the mixed layer and the interior. In (5), the mixed layer temperature is in equilibrium (T_E) with the ice-ocean and interior-mixed layer heat fluxes [Lane-Serff,

1995]; T_E indicates the relative magnitude of γ_T and e' .

In the limit of rapid latent heat flux ($\gamma_T \gg e'$), the temperature of the mixed layer approaches the freezing point; the rate of entrainment limits melting. If γ_T and e' are of the same magnitude, not all of the heat entrained into the mixed layer is transferred to the ice. Importantly, if γ_T and e' have a different dependence on physical constraints (e.g. slope), the ratio in (5) will vary spatially, driving horizontal gradients in mixed layer temperature and melting.

Defining efficiency

In this paper, sub-ice shelf (internal) control of oceanic heat is assessed at two barriers: the base of the mixed layer and the ice-ocean interface (#3 and #4 in figure 1). At each location, quantities may be defined to assess the efficiency: here, they are denoted as the entrainment efficiency (f_E) and the ice-ocean efficiency (f_I), respectively.

If interior water properties are uniform, there are no sources of heat underneath the ice shelf other than the ice, and diffusive heat fluxes are negligible, the entrainment efficiency is simply the volume fraction of interior water entrained into the mixed layer. In a steady state,

$$f_E = \frac{\int_{x_E}^{x_W} \int_{y_S}^{y_N} e' dy dx}{\int_{y_S}^{y_N} u^+(x_w) h_D(x_w) dx} \quad (6)$$

where y_N , y_S , x_E , and x_W are the boundaries of the ice shelf, u^+ is the zonal velocity evaluated only where $u > 0$, and h_D is the thickness of the interior layer.

Heat entrained into the mixed layer may be used at any location along the ice

shelf. This heat flux, the total available for melting, can be expressed as:

$$q_T = -e' \Delta T_T (7)$$

where the overall thermal driving is $\Delta T_T = \Delta T_I + \Delta T_M = T_B - T_D$. A variable freezing point can be incorporated by defining q_T^{MAX} as the maximum available heat for melting, where $\Delta T_T^{MAX} = T_B^{MIN} - T_D$, and T_B^{MIN} is the minimum freezing point along the ice shelf. Since $\Delta T_T^{MAX} > \Delta T_M$ (unless the mixed layer is supercooled), in a local balance (5), entrainment delivers an excess of heat for basal melting. Due to the pressure dependence of the freezing point [Millero, 1978], this excess will increase if water is advected upslope (freshening of the boundary layer may offset this effect).

Along the zonal axis of the ice shelf, assuming the mixed layer flows upslope, the excess heat flux (H_X) is:

$$H_X(x) = \int_{X_E}^x (Q_T^{MAX} + Q_I) dx (8)$$

where meridionally integrated heat fluxes are given in capital letters. The gradient of excess heat along the ice shelf is:

$$\frac{dH_X}{dx}(x) = (Q_T^{MAX} + Q_I) (9)$$

Integrated over the ice shelf, the fraction of entrained heat used for melting is:

$$f_I(x_w) = \left[1 - \frac{H_X(x_w)}{\int_{x_E}^{x_w} \int_{y_S}^{y_w} Q_T^{MAX} dy dx} \right] (10)$$

and the overall efficiency of melting (f_O) is:

$$f_O = f_E f_I(x_w) (11)$$

In subsequent sections, we use a numerical model to examine the magnitude and

spatial distribution of mixed layer heat fluxes, which influence the efficiency of melting and its sensitivity to ice shelf morphology and ocean temperature.

NUMERICAL MODEL

Simulations were performed with the Hallberg Isopycnal Model [Hallberg and Gnanadesikan, 2006], a Boussinesq, 3-D, numerical ocean model. The model incorporates the barriers to heat transfer (#3 and #4 in Figure 1) using a bulk mixed layer [Hallberg, 2003] and a thermodynamic parameterization of ice-ocean fluxes [Little, et al., 2008] (after the 3-equation formulation of Holland and Jenkins [1999]). A local turbulent kinetic energy (TKE) balance determines the rate of entrainment. The mixed layer shoals in response to ice shelf melting and deepens with increasing shear, scaling with the Monin-Obhukhov lengthscale [Niiler and Kraus, 1977]. Shear production of TKE is calculated using a quadratic drag law employing a spatially and temporally fixed drag coefficient of 2.5×10^{-3} . Interior and non-local mixing may be addressed using additional parameterizations [Hallberg, 2000; Jackson, et al., 2008]; given the limited vertical resolution, these were not included in these simulations.

The morphological details of ice shelves vary due to local bedrock topography and embayment shape, which modify the stress balance and thus the ice shelf thickness and flow rate. Spatially comprehensive, accurate ice thickness measurements are difficult to obtain without concerted effort [Corr, et al., 2002]. Yet it is known that the aspect ratio of ice shelves, even within the Amundsen Sea, varies considerably; from confined, narrow, deep ice shelves (Pine Island Ice Shelf, or PIIS, $\sim 2300 \text{ km}^2$) to large ice shelves covering multiple embayments (Getz Ice Shelf, $>30000 \text{ km}^2$) [Shepherd, et al., 2004].

These ice shelves exhibit strong longitudinal (along-ice flow) thickness gradients; near grounding lines, basal slope may be an order of magnitude larger than tens of kilometers down-glacier [Corr, *et al.*, 2001].

In the numerical simulations, the principal configuration (BASE) aims to reproduce key large-scale aspects of PIIS; it features a zonally uniform bathymetric trough (maximum depth 900 m) that is intersected by a meridionally uniform ice shelf (figure 3a,b). The depth of the ice shelf base (B) as a function of distance to the east (x , in m) is described by:

$$B = \min\left\{240, \frac{\alpha_1}{\left(\alpha_2 - \frac{x}{1000}\right)^{2.5}}\right\} \quad (12)$$

where $\alpha_1 = 2200$ and $\alpha_2 = 106$.

The slope of the BASE case thus varies from 0.06 at the deepest location in the domain ($x = 100$ km) to near zero at 20 km. This shape is smaller and steeper than those used in other idealized studies [HJH08; Walker, *et al.*, 2008], and defines a grounding line that circumscribes the ice shelf cavity. To illuminate slope- and scale-driven control of basal melting, alternate ice shelf aspect ratios are examined (described in table 1 and figure 3c-f). In all configurations, the minimum water column thickness is 10 meters.

All simulations are initialized with a 10 meter thick mixed layer at the in-situ freezing point and an interior layer initialized at a fixed temperature (T_D) that varies between -2.0°C to 1.5°C across simulations; the salinity of the interior is always 34.9 psu. Buoyancy-driven flow and tracer properties evolve under the ice shelf over 60 days. Near the western boundary, layer interfaces and properties are restored to initial values. To mitigate any effects of the applied restoring, only the eastern 3/5 of the domain is

analyzed (the “analysis region”). In all model runs, the kinetic energy of the ocean stabilizes after ~20 days.

The ice shelf is non-dynamic, implying a steady local mass balance. Heat conduction into the ice is described by an advective/diffusive heat balance [Holland and Jenkins, 1999]; the interior ice temperature is assumed to be -15°C. No ice shelf front or open ocean is included; simulations with a portion of the domain outside of the ice shelf cavity did not change the nature of the results.

RESULTS

Oceanic heat initiates differential melting that, when coupled to the circulation, establishes the steady-state mixed layer hydrography, flow, and heat fluxes illustrated for the BASE case ($T_D=1.0^\circ\text{C}$) in figures 4a-c. Gradients in ΔT_I are driven by ocean temperature, rather than the in-situ freezing point, which varies little underneath the ice shelf; salinity-dependent changes in the freezing point compensate for its pressure-dependence. Temperatures are highest near the grounding line, reaching a maximum of 0.1°C ($\Delta T_I^{\text{max}}=1.93^\circ\text{C}$). Since the mixed layer is comprised solely of interior water and ice shelf meltwater, salinity gradients are proportional to those of temperature [Gade, 1979]. Though the meltwater fraction by volume is relatively small (≤ 25 ppt), especially near cavity boundaries, melting cools and freshens the mixed layer; the addition of buoyancy drives a southwestward frictional-geostrophic flow [Price and Baringer, 1994]. Mixed layer thicknesses are generally less than 10 meters, with regions near boundaries less than 2 meters. There is little meridional (transverse to the ice flow) variation in oceanic properties or melting rates, except adjacent to the southern boundary, where flow

converges.

High mixed layer temperatures coincide with maximal rates of entrainment ($e' \sim 4000 \text{ myr}^{-1}$) of interior water. Despite ongoing entrainment of heat, the mixed layer cools as it flows upslope, reaching -1.4°C approximately 30 kilometers from the grounding line. Along flow paths, temperature decreases monotonically; the velocity profile is more complex. Two factors contribute to the relatively constant flow speed ($\sim 0.20 \text{ ms}^{-1}$) over the western 30 km of the domain: 1) as meltwater accumulates upslope, density and slope contributions to the pressure gradient compensate; 2) near the deepest part of the ice shelf, frictional drag is larger due to the thin mixed layer. Flow speed and turbulent mixing are coupled, increasing in tandem until decreasing slope acts to weaken the pressure gradient. As a result of the spatial decorrelation of temperature and velocity, melting rates -- driven by the product of these properties (3) -- are maximized over a broad region approximately 5-10 km from the grounding line. The maximum melting rate is 49 myr^{-1} ; it is shifted upslope of the entrainment maximum.

Mixed layer dynamic regimes

To examine these strong zonal gradients in mixed layer temperature and salinity, it is useful to divide the cavity into three regions: the *initiation* region, here, defined to be within 5 km of the deepest point of the ice shelf; the *maintenance* region, between 70 and 95 km; and the *outflow* region, west of 70 km. The regions are differentiated by their heat balance (figure 4d): slope-driven changes in the rate of entrainment, flow speed, and mixed layer thickness control local temperature and importance of advection. Although these regimes share characteristics with those described by Lane-Serff [1995], the mixed

layer dynamics in these 3-D simulations differ.

In the initiation region, the flux of heat available for melting (Q_T) rapidly increases to several times larger than the ice-ocean heat flux (Q_I), driving high mixed layer temperatures (T) and rapid accumulation of heat (H_X). Here, where a local heat balance (5) is applicable, the partitioning of the ice-interior temperature gradient ($\Delta T_T^{900m} \sim -3.3^\circ\text{C}$, $\Delta T_I^{900m} \sim -1.9^\circ\text{C}$) indicates that e' exceeds γ_T .

In the maintenance region, Q_T decreases rapidly; advection ($Q_A=Q_I+Q_E$) moves heat upslope, smoothing temperature gradients driven by the shape of the ice shelf. Since a non-negligible advective heat flux is maintained, the heat balance is better described by (4). Including non-local contributions to the heat balance increases ΔT_I relative to (5) (i.e. $T > T_E$); ice-ocean heat flux (Q_I) increases in proportion to the advected anomaly, $T - T_E$, cooling the mixed layer. As a parcel rises along the (thinning) ice shelf, decreasing entrainment (19) acts to increase Q_I relative to Q_T ; mixed layer cooling opposes this tendency. The transition between accumulation and use of heat (where $Q_T = -Q_I$ and $\partial H_X / \partial x = 0$) occurs approximately 15 km from the grounding line in the BASE configuration; it is controlled by local slope (which drives e' / γ_T) and the upstream morphology (which controls advected heat, and thus gives $\Delta T_I / \Delta T_T$).

In the outflow, Q_I exceeds Q_E , but heat fluxes are greatly reduced compared to regions of higher slope. The decay of excess heat ($\partial H_X / \partial x$) decreases sharply as southward flow converges; even though the mixed layer temperature is higher than a local heat balance dictates, it relaxes only slowly towards the freezing point. In the BASE simulation, Q_I exceeds Q_E along the entire extent of the maintenance and outflow regions; the decay of excess heat is incomplete. In aggregate, these regimes conspire to

trap previously entrained heat in the mixed layer (which exits the analysis region at approximately -1.5°C , well above the local freezing point), so that the area-integrated ice-ocean efficiency (f_I) is 87%.

Shape and temperature sensitivity

Changes in the interior temperature, aspect ratio, or the area of the ice shelf do not change the nature of the three regimes (figure 5). Meridional variability remains weak; changes in the ice shelf aspect ratio add more, longer, or steeper flow paths along the ice shelf base. The results obtained for alternate forcing and shape scenarios are summarized in table 2; they indicate that ice shelf slope controls the entrainment of heat, the efficiency with which it is used, and the distribution of basal melting.

In all simulations, melting is heavily weighted towards deeper parts of the ice shelf, despite two features of these simulations that may limit the zonal gradient of melting: the ice shelves' decreasing areal extent in deeper regions and a limited representation of stratification in the upper water column. Maximum melting rates (m'_{MAX}), always located near the deepest part of the ice shelf, are 2.6 to 10.3 times higher than melting rates ($\overline{m_O'}$) averaged over the analysis region.

Steeper ice shelves have a higher mean melting rate; area-averaged power laws of the form $\overline{m_O'} = c\theta^n$ give an exponent of 0.94 to 1.15 (dependent on the interior temperature). However, basal melting's sensitivity to slope is hidden by spatial inhomogeneity (figure 6). In the initiation region, slope-dependent basal melting power laws ($\overline{m_I'} = c\theta^n$) give an exponent of 1.21 to 1.37 (for each interior temperature, the exponent is larger in the initiation region than averaged over the analysis region).

All configurations show a common, super-linear response to increasing ocean temperature, although the exact dependence differs; the details of morphology influence the response to temperature (figure 7). Area-averaged melting rates obtained over a temperature range $-2.0^{\circ}\text{C} \leq T_D \leq 1.5^{\circ}\text{C}$ show negative deviations from a quadratic scaling – which is consistent with earlier numerical studies [HJH08]. Power laws of the form $\overline{m_O} = c(\Delta T_T)^n$ give an exponent of 1.55 to 1.81.

The slope-dependence of entrainment is more pronounced than that of melting, driving increases in advection; as temperature and slope in the initiation region increase, f_I declines and distribution of melting shifts seaward. Advective heat loss increases steadily with thermal driving for all cavity shapes (shown for the BASE case in figure 8). Incomplete cooling drives a decrease in ice-ocean efficiency, driving divergence from a quadratic scaling.

In these simulations, the efficiency of entrainment (f_E) is always below 55%, indicating a significant amount of heat is recirculated underneath the ice shelf, however, it does not exhibit strong trends with temperature or ice shelf shape.

DISCUSSION

These results indicate that basal slope controls the entrainment of heat, but that ice-ocean boundary layer heat transfer may alter the relationship between melting and slope; these processes also govern the response of melting to ocean temperature. The underlying physics, as well as their implications for modeling and observational efforts, are discussed below.

On the local slope dependence of the melting rate

The slope dependence of turbulent entrainment may be examined using energetic considerations. Mechanical energy derived from surface stress at the ice interface mixes the local meltwater flux and entrained interior water:

$$\frac{u_*^3}{\kappa} = \frac{h}{2}(-\beta g e' \Delta S_M + B_0) \quad (13)$$

where u_* is the friction velocity (ms^{-1}), h is the thickness of the mixed layer (m), κ is Von Karman's constant, g is the acceleration due to gravity (ms^{-2}), β is the salinity contraction coefficient, $\Delta S_M = S - S_D$ is the salinity difference across the base of the mixed layer, S_D is the salinity of the interior (psu), and B_0 is the buoyancy flux at the ice-ocean interface (m^2s^{-3}). Ignoring thermal expansion and meltwater input, the buoyancy flux is given by:

$$B_0 \approx -\beta g m' S \quad (14)$$

The local salt balance in the mixed layer is:

$$e' = \frac{m' S}{\Delta S_M} \quad (15)$$

Combining (12)-(14):

$$\frac{u_*^3}{\beta \kappa g h} \approx e' \Delta S_M \quad (16)$$

Scaling (16), letting $u_* \sim U \sim \Delta S \sin \theta \sim \Delta S \theta$, where θ is the angle if the ice shelf's lower surface with respect to a geopotential surface,

$$E \sim \frac{\Delta S^2 \theta^3}{H} \quad (17)$$

A scaling for H must be consistent with mass conservation, i.e.:

$$E \sim \frac{UH}{L} \quad (18)$$

suggesting that $H \sim U$ and $E \sim U\theta$. This dependence is captured in the simple form for entrainment [Pedersen, 1980] employed in HJH08 and Jenkins [1991]:

$$e' = c_E |u| \sin \theta \quad (19)$$

where c_E is an empirical constant; it is also consistent with a Richardson number scaling: in a buoyancy-driven current, for any density gradient, flow speed increases with slope.

In the BASE simulation, e' is poorly predicted by flow speed (figure 9a), but improves upon introducing the local slope (figure 9b), implying that the form of (19) is adequate. Using (3), (5), and (19), the control of mixed layer temperature and melting rates can be expressed in terms of the overall thermal driving (ΔT_T).

$$\Delta T_I = \left(\frac{\gamma_T}{e'} + 1 \right)^{-1} \Delta T_T \quad (20)$$

$$m' \propto \frac{\gamma_T e'}{\gamma_T + e'} \Delta T_T \quad (21)$$

The magnitude of e' and γ_T determines the sensitivity to slope. Although e'/γ_T varies over the ice shelf, numerical simulations indicate that this ratio is $O(1)$ over most of the domain. Assuming $U \sim \theta$, and using (19), $\gamma_T \sim \theta$ and $e' \sim \theta^2$. A scaling for mixed layer temperature and melting rate in a local heat balance is then given by:

$$T \sim \frac{\theta}{1 + \theta} \quad (22)$$

$$m' \sim \frac{\theta^2}{1 + \theta} \quad (23)$$

In figure 6, e' approaches a quadratic dependence with slope (expected if $U \sim \Delta S \theta$), while γ_T shows a slight negative departure from linearity [Holland and Jenkins, 1999]. As predicted by (23), the numerical model confirms a slope-dependence of basal melting intermediate between that of e' and γ_T ; mixed layer temperature exhibits a weaker

dependence, as predicted by (22).

These simulations suggest that the parameterization of entrainment is important in large-scale models, especially the nature of its divergence from the ice-ocean exchange velocity. Though buoyancy fluxes affect this ratio, they drive e' and γ_T in the same direction. Slope should be expected to drive large variations in (5); even weak dependence will drive substantial spatial variability under realistically shaped ice shelves.

The role of advection and efficiency

The presence of subsurface meltwater-freshened water masses substantially above the surface freezing point near ice shelves in the Bellinghousen [Jenkins and Jacobs, 2008] and Amundsen [Jacobs, et al., 1996] Seas suggests that heat near the ice-ocean interface is unused. The simulations described here indicate that this inefficiency is driven by the slow decay rate of advected thermal anomalies ($T - T_E$) originating in regions of higher slope.

The temperature of outflow (-1.5°C) is insensitive to ice shelf shape; ice-ocean heat flux is controlled primarily by the thickness of the mixed layer, rather than the distance traveled along the ice shelf base. A minimum decay lengthscale for excess heat can be examined by assuming: 1) the relatively small meltwater fraction does not change the volume or temperature of the plume; 2) T_B , h , and basal slope are constant along the ice shelf and 3) a constant drag coefficient and a weak dependence of γ_T on buoyancy flux [HJH08], i.e.:

$$\gamma_T = g_T |u| \quad (24)$$

where $|u|$ is the flow speed and g_T is a constant transfer velocity. (4) may then be

rewritten:

$$\frac{dT}{ds} = \frac{1}{h}(g_T \Delta T_I - c_E \Delta T_M) \quad (25)$$

where c_E is a constant that includes the (constant) slope. For simplicity, we assume h and T_B are constant. In (25), a thermal anomaly will decay toward T_E with an e-folding length scale that is solely a function of the layer thickness and the transfer velocity. For $c_E = g_T = 4 \times 10^{-4}$ and $2 < h < 10$ meters, the initial thermal forcing decays exponentially over 40 to 200 km, indicating that advective heat loss is likely.

Mixed layer cooling is further slowed by downstream convergence. Using a 2-D plume model, Lane-Serff [1995] observed that the layer thickness along the flow path of an entraining plume controls its dependence on the ice-ocean heat flux: a thicker layer decreases the cooling rate. Here, in 3-D simulations, horizontal flow convergence drives the retention of mixed layer heat. Since the frictional-geostrophic current in this simulation flows southwest (figure 4b), with an upslope turning angle dependent on friction, the southern boundary forces convergence. If there is no entrainment or detrainment from the mixed layer, mass is conserved in the outflowing boundary current:

$$\frac{VH_M}{L_M} \sim \frac{UH_O}{L_O} \quad (26)$$

Scales for velocity, layer thickness, and the width of the maintenance region are given by V , H_M , and L_M respectively; those for the outflow region are given by U , H_O , and L_O . Velocity scales can be derived for boundary currents and geostrophic flow, but are functions of slope, which varies greatly in these experiments. In figure 4b, flow speed in the outflow and maintenance regions are similar. Assuming U and V are equivalent in (26), the thickness of the outflow is determined by the widths of the boundary current and

the dimensions of the ice shelf. The width of an outflowing boundary current can be estimated [Little, et al., 2008]; generally, it will be less than that of the ice shelf, driving convergence.

With the simplified morphology employed here, side boundaries drive convergent flow, however, smaller scale sub-ice basal features (channels) may also act to channel outflow; the relevance of the outflow dynamics may not be limited to simplified domains. The importance of flow convergence to melting implies that a 2-D (x-z) approach along the ice shelf flow may be limited, even in the absence of small-scale features.

How efficiency affects basal melting's sensitivity to temperature

The zonal distribution of heat fluxes in the BASE case (figure 10a) indicates that entrained heat in the initiation and maintenance regions increases with interior temperature, yet a substantial fraction is unused. If a mixed layer with an initial thermal anomaly ($T > T_E$) flows along the ice shelf without further entrainment, (25) can be integrated to describe the temperature along a flow path:

$$T(x) = [T_0 - T_E] e^{-\frac{(c_E + g_T)}{h} x} + T_E \quad (27)$$

Defining ΔT as the temperature drop across the region of advective influence, and T_0 as the maximum mixed layer temperature attained in the initiation region (assumed to be in a local heat balance, where $T_0 \sim T_D$):

$$\Delta T \sim \Delta T_D e^{-\frac{g_T}{h} x} \quad (28)$$

Where advective heat flux is non-negligible, the local thermal response to sub-ice shelf warming is a fraction of the increase in the initiation region: cooling occurs gradually over the ice shelf. If mixed layer dynamics do not change dramatically with

interior temperature, some of the increase in entrained heat remains in the mixed layer as it escapes the ice shelf. Meridionally averaged temperature profiles from the numerical results (figure 10b) support this simple analysis – the local response is constant over the range in interior temperature, and the temperature of the mixed layer at the ice shelf front increases by 0.6°C over a 1.5°C range in T_D .

In determining the sensitivity of basal melting to ocean temperature, *HJH08* assumes all heat in the well-mixed layer beneath the ice shelf is used for melting ($f_M=1$). When melting is limited by ice-ocean heat flux (γ), a scaling law based on entrainment will not be valid. Only a fraction of entrained heat is used. Because this fraction decreases with temperature, area-integrated melting and entrainment exhibit a differing sensitivity to ocean thermal forcing.

Implications for simple models and parameterizations of basal melting

The slope-dependent dynamics explored here may inform efforts to develop simple models that represent 1) patterns of basal melting along the longitudinal axis of an ice shelf [*Walker, et al.*, 2008] and 2) aggregated ice-ocean heat and freshwater fluxes [*Beckmann and Goosse*, 2003]. Although the principal configuration and oceanographic conditions examined here were chosen with reference to the Amundsen Sea, the large range of thermal forcing and shapes employed in the numerical simulations imply that these findings may be more broadly applicable.

For glaciological considerations, sharp, slope-driven, spatial gradients in temperature, velocity, and melting imply that an area-averaged representation will not adequately characterize basal melting (or its response to climate). Given that much of the

493 ice shelf contributes very little to basal melting, efforts should focus on deeper, steeper
494 portions of the ice shelf.

495 Yet even over subsections of the ice shelf, developing a generalized relationship
496 that accounts for spatial variable dynamics poses difficulties. As the majority of ice shelf
497 melting in these simulations occurs in the maintenance region, accounting for non-local
498 heat sources may be required to estimate the longitudinal distribution of melting.

499 Additionally, the local melting rate is a function of both the thermal forcing and the flow
500 speed (3). Simple basal melting models require spatially-correlated rates of increase for
501 these variables. Prior efforts to develop scaling laws have used a meltwater-dependent
502 geostrophic approximation to account for flow speed. However, these simulations do not
503 show a clear salinity-flow speed relationship, due to the spatially varying slope and
504 frictional effects in thin mixed layers and near side boundaries.

505 Ignoring advective heat fluxes, the simplest model for temperature and basal
506 melting (20-23) requires a functional form for e' and γ_r that captures their slope-
507 dependence and relative magnitudes, underscoring the need for observational validation
508 of these parameters.

509 The distribution of melting under an ice shelf may be less relevant for large-scale
510 climate modeling, in which integrated ocean-cryosphere heat and freshwater fluxes are
511 paramount. Strong slope-dependence of entrainment, melting, and ice-ocean efficiency
512 influences these integrated quantities. In these simulations, integrated heat fluxes are
513 more dependent upon the local response to slope than changes in efficiency, but the
514 absolute magnitude of each effect will depend strongly on oceanographic conditions and
515 the details of the ice shelf shape. At a minimum, these findings suggest that models

seeking to connect far-field subsurface ocean temperatures to aggregate basal melting rates should account for the gradient in basal slope muted by an efficiency factor that is dictated by the large-scale morphology and thermal forcing.

This paper demonstrates that ice shelf shape and subsurface temperature control melting rates, and that they are inter-dependent. This poses difficulties for the development of simple scaling relationships on an integrated basis, i.e. of the form:

$$m' = f_O \theta^{n_1} \Delta T_T^{n_2} \quad (29)$$

where f_O is an ice shelf efficiency factor, n_1 is the sensitivity to slope, and n_2 is the sensitivity to temperature. Because these exponents are functions of the ice-ocean efficiency, melting may have a complex dependence on morphology and oceanographic conditions. Additionally, these results do not indicate a consistent relationship between integrated melting rates and overall efficiency. As temperature and shape are changed, changes in the entrainment efficiency (f_E) and the import of heat into the ice shelf are non-linear; additional heat for melting is not derived exclusively from either. Since the heat flux into the ice shelf cavity is a slave to the buoyancy forcing in these simulations, a detailed investigation of the dynamics controlling heat flux at the ice shelf front is not possible. The interaction of internal efficiency, the coupled melting/inflow response, and external heat sources deserves further investigation.

Perhaps more promising than the development of a precise scaling law are studies that investigate the magnitude and timescale of the glaciological response to external (subsurface temperature) and internal (ice shelf morphology) perturbations. Defining regions of ice shelves that are critical to ice shelf stability will also narrow the potential range of responses.

539

540 ***The basal slope feedback***

541 Walker et al. [2008] analyzed the role of a fixed distribution of basal melting on
542 grounding line retreat, determining that increased rates near grounding lines were of
543 comparable importance to large changes in the area-averaged melting; basal melting
544 gradients changed the ice shelf profile, grounding line location, and the behavior of the
545 grounded ice upstream.

546 The results discussed here suggest an instability in the coupled ice-ocean system
547 (the “basal slope feedback”) if the distribution of melting is allowed to vary as a function
548 of ice shelf slope; an intensification of local and cavity-wide melting rates driven by
549 steeper ice shelves may further increases basal melting rates. The initial perturbation may
550 be a change in ocean temperature, but it could also be initiated by a change in grounding
551 line ice flux or the stress regime of the ice shelf.

552 The coupled response to enhanced entrainment and melting will govern the nature
553 and strength of the basal slope feedback. The change in oceanographic conditions under
554 different ice shelves suggests at least two possibilities. Steeper slopes may increase the
555 heat content of the mixed layer and accelerate the flow, particularly near ice shelf
556 grounding lines. With these ocean-only simulations, increased local melting implies that
557 the ice shelf may assume a more concave shape [*Walker and Holland, 2007*]. Although
558 the local effect of a steeper slope dominates the response of efficiency in these
559 simulations, it is possible that in a different parameter space, decreases in efficiency
560 could shut off the feedback. Ocean dynamics will be strongly influenced by the
561 glaciological response to changes in melting, reinforcing the need for the development

and assessment of a hierarchy of coupled ice-ocean models.

CONCLUSIONS

In these simulations, large-scale ice shelf thickness gradients foster mixed layer dynamic regimes that control the location and rate of basal melting. Strong, slope-dependent entrainment enhances melting in steep regions; yet inefficiencies are present that limit the use of sub-ice shelf oceanic heat under thinner, less steeply-sloped regions of the ice shelf.

In a local heat balance, the mixed layer temperature and melting rate is determined by the ratio of the entrainment rate and the ice-ocean thermal exchange velocity. This ratio also governs the local sensitivity of basal melting to slope and interior ocean temperature. Given the importance of advective heat fluxes and the idealized nature of these simulations, a precise dependence of melting on slope is not presented, yet these results indicate that ice shelf thickness gradients drive comparable along-ice flow gradients in basal melting. A super-linear dependence of melting is evident under the deepest, fastest-melting part of ice shelves. Ice shelves thus entrain heat and melt disproportionately in steep regions, and they are most sensitive to changes in ice shelf slope in locations that have high basal melting rates. The disproportionate influence of narrow *initiation* regions near the grounding line underscores the importance of oceanographic constraints on mixing under steeper parts of ice shelves; for models, accurate turbulence parameterizations and an assessment of their sensitivity to spatial resolution are critical.

The use of entrained heat is limited by flow convergence, a key feature of the *outflow* regime. Because mixed layer flow converges rapidly in these simulations, outflowing seawater has a temperature above the in-situ freezing point; it is more sensitive to the interior temperature and the thickness of the mixed layer than the dimensions of the ice shelf. Defining ice-ocean efficiency as the fraction of entrained heat transferred to the ice allows its sensitivity to shape, scale, and temperature to be quantified. Because latent cooling lags increases in entrained heat, ice-ocean efficiency decreases with increasing ocean temperature; the deviation of previous modeling studies from a simple scaling law may result from this advective heat loss.

These simulations indicate that internal dynamics -- especially ice shelf shape -- exert an influence on basal melting rates that is comparable to that of oceanographic properties outside the ice shelf cavity. Only 20-50% of sub-ice shelf heat is used for melting; small changes in efficiency may modify the response to a change in oceanic forcing. Ice shelf morphology should thus be addressed in climate model parameterizations and in the (presumably more detailed) representation of basal melting incorporated in ice shelf/ice sheet models. The importance of the physics introduced here are scale-dependent; an assessment of each modeling community's needs, and comparison with observations, are required to extend these findings toward useable parameterizations.

604 **ACKNOWLEDGEMENTS**

605 Doug MacAyeal, Torge Martin, Stan Jacobs, and Rachael Mueller contributed
606 helpful guidance on earlier versions of this manuscript. CML receives research funding
607 from the United States Environmental Protection Agency (EPA) Science to Achieve
608 Results graduate fellowship program, GFDL (through the Cooperative Institute for
609 Climate Science), and the Science, Technology, and Environmental Policy program in the
610 Woodrow Wilson School of Public and International Affairs at Princeton University.
611 EPA has not officially endorsed this publication and the views expressed herein may not
612 reflect the views of the EPA.

REFERENCES

- Beckmann, A., and H. Goosse (2003), A parameterization of ice shelf-ocean interaction for climate models, *Ocean Model*, 5, 157-170.
- Corr, H. F. J., C.S.M Doake, A. Jenkins, and D.G. Vaughan (2001), Investigations of an "ice plain" in the mouth of Pine Island Glacier, Antarctica, *J Glaciol*, 47, 51-57.
- Corr, H. F. J., A. Jenkins, K.W. Nicholls, and C.S.M Doake (2002), Precise measurement of changes in ice-shelf thickness by phase-sensitive radar to determine basal melt rates, *Geophys Res Lett*, 29, doi:10.1029/2001GL014618.
- Dupont, T. K., and R. B. Alley (2005), Assessment of the importance of ice-shelf buttressing to ice-sheet flow, *Geophys Res Lett*, 32, doi:10.1029/2004GL022024.
- Dupont, T. K., and R. B. Alley (2006), Role of small ice shelves in sea-level rise, *Geophys Res Lett*, 33, doi:10.1029/2005GL025665.
- Ellison, T. H., and J. S. Turner (1959), Turbulent Entrainment In Stratified Flows, *J Fluid Mech*, 6, 423-448.
- Gade, H. G. (1979), Melting of Ice in Sea-Water - Primitive Model with Application to the Antarctic Ice Shelf and Icebergs, *J Phys Oceanogr*, 9, 189-198.
- Grosfeld, K., and H. Sandhager (2004), The evolution of a coupled ice shelf-ocean system under different climate states, *Global And Planetary Change*, 42, 107-132.
- Hallberg, R. (2003), The suitability of large-scale ocean models for adapting parameterizations of boundary mixing and a description of a refined bulk mixed layer model, paper presented at *Near Boundary Processes and Their Parameterization: Proc.*

Little et al.

2003 'Aha Huliko'a Hawaiian Winter Workshop, Honolulu, HI, University of Hawaii at Manoa, 187-203.

Hallberg, R. (2000), Time integration of diapycnal diffusion and Richardson number-dependent mixing in isopycnal coordinate ocean models, *Mon Wea Rev*, 128, 1402-1419.

Hallberg, R., and A. Gnanadesikan (2006), The role of eddies in determining the structure and response of the wind-driven southern hemisphere overturning: Results from the Modeling Eddies in the Southern Ocean (MESO) project, *J Phys Oceanogr*, 36, 2232-2252.

Hohmann, R., P. Schlosser, S. Jacobs, A. Ludin, R. Weppernig (2002), Excess helium and neon in the southeast Pacific: Tracers for glacial meltwater, *J Geophys Res-Oceans*, 107, doi:10.1029/2000JC000378.

Holland, D. M., and A. Jenkins (1999), Modeling thermodynamic ice-ocean interactions at the base of an ice shelf, *J Phys Oceanogr*, 29, 1787-1800.

Holland, D. M., and A. Jenkins (2001), Adaptation of an isopycnal coordinate ocean model for the study of circulation beneath ice shelves, *Mon Wea Rev*, 129, 1905-1927.

Holland, P. R., and D. L. Feltham (2005), Frazil dynamics and precipitation in a water column with depth-dependent supercooling, *J Fluid Mech*, 530, 101-124.

Holland, P. R., A. Jenkins, and D.M. Holland (2008), The response of ice shelf basal melting to variations in ocean temperature, *J Climate*, 21, 2558-2572.

Jackson, L., R. Hallberg, and S. Legg (2008), A parameterization of shear-driven turbulence for ocean climate models, *J Phys Oceanogr*, 38, 1033-1053.

Little et al.

Jacobs, S. S., H.H. Hellmer, and A. Jenkins (1996), Antarctic ice sheet melting in the Southeast Pacific, *Geophys Res Lett*, *23*, 957-960.

Jenkins, A. (1991), A One-Dimensional Model of Ice Shelf-Ocean Interaction, *J Geophys Res-Oceans*, *96*, 20671-20677.

Jenkins, A., and S. Jacobs (2008), Circulation and melting beneath George VI Ice Shelf, Antarctica, *J Geophys Res-Oceans*, *113*, C04013, doi:04010.01029/02007JC004449.

Jiang, L., and R. Garwood (1998), Three-dimensional simulations of overflows on continental slopes, *J Geophys Res-Oceans*, *103*, 5459-5476.

Joughin, I., and L. Padman (2003), Melting and freezing beneath Filchner-Ronne Ice Shelf, Antarctica, *Geophys Res Lett*, *30*, doi:10.1029/2003GL016941.

Kader, B. A., and A. M. Yaglom (1972), Heat and Mass-Transfer Laws for Fully Turbulent Wall Flows, *Int J Heat Mass Tran*, *15*, 2329-2351.

Kader, B. A., and A. M. Yaglom (1977), Turbulent Heat and Mass-Transfer from a Wall with Parallel Roughness Ridges, *Int J Heat Mass Tran*, *20*, 345-357.

Lane-Serff, G. F. (1995), On Meltwater Under Ice Shelves, *J Geophys Res-Oceans*, *100*, 6961-6965.

Legg, S., R. Hallberg, and J.B. Girton (2006), Comparison of entrainment in overflows simulated by z-coordinate, isopycnal and non-hydrostatic models, *Ocean Model*, *11*, 69-97.

Little, C. M., A. Gnanadesikan, and R. Hallberg, (2008), Large scale oceanographic constraints on the distribution of melting and freezing under ice shelves, *J Phys Oceanogr*, *38*, 2242-2255.

Little et al.

Little, C. M., Little, C.M., M. Oppenheimer, R.B. Alley, V. Balaji, G.K.C. Clarke, T.L. Delworth, R. Hallberg, D.M. Holland, C.L. Hulbe, S. Jacobs, J.V. Johnson, H. Levy, W.H. Lipscomb, S.J. Marshall, B.R. Parizek, A.J. Payne, G.A. Schmidt, R.J. Stouffer, D.G. Vaughan, and M. Winton (2007), Toward a new generation of ice sheet models, *Eos Trans. AGU*, 88, doi:10.1029/2007EO520002.

MacAyeal, D. R. (1984), Thermohaline Circulation Below the Ross Ice Shelf - a Consequence of Tidally Induced Vertical Mixing and Basal Melting, *J Geophys Res-Oceans*, 89, 597-606.

Makinson, K. (2002), Modeling tidal current profiles and vertical mixing beneath Filchner-Ronne Ice Shelf, Antarctica, *J Phys Oceanogr*, 32, 202-215.

McPhee, M. G. (1992), Turbulent heat-flux in the upper ocean under sea ice, *J Geophys Res-Oceans*, 97, 5365-5379.

McPhee, M. G. (1999), Parameterization of mixing in the ocean boundary layer, *J Marine Syst*, 21, 55-65.

Mellor, G.L., M.G. McPhee, and M. Steele (1986), Ice-seawater turbulent boundary layer interaction with melting or freezing, *J Phys Oceanogr*, 16, 1829–1846.

Millero, F. (1978), Freezing point of seawater, 29-31 pp, UNESCO Technical Papers Marine Science, Appendix 6.

Nicholls, K. W., Abrahamsen, E. P., Buck, J. J. H., Dodd, P. A., Goldblatt, C., Griffiths, G., Heywood, K. J., Hughes, N. E., Kaletsky, A., Lane-Serff, G. F., McPhail, S. D., Millard, N. W., Oliver, K. I. C., Perrett, J., Price, M. R., Pudsey, C. J., Saw, K., Stansfield, K., Stott, M. J., Wadhams, P., Webb, A. T., Wilkinson, J. P. (2006),

Little et al.

Measurements beneath an Antarctic ice shelf using an autonomous underwater vehicle, *Geophys Res Lett*, 33, doi:10.1029/2006GL025998.

Nicholls, K. W., S. Osterhus, K. Makinson, and M.R. Johnson (2001), Oceanographic conditions south of Berkner Island, beneath Filchner-Ronne Ice Shelf, Antarctica, *J Geophys Res-Oceans*, 106, 11481-11492.

Niiler, P. P., and E. B. Kraus (1977), One-dimensional models of the upper ocean thermocline, in *Modelling and Prediction of the Upper Layers of the Ocean*, edited by E. B. Kraus, pp. 143-172, Pergamon Press.

Orsi, A. H., G.C. Johnson, and J.L. Bullister (1999), Circulation, mixing, and production of Antarctic Bottom Water, *Prog Oceanogr*, 43, 55-109.

Padman, L., H.A. Fricker, R. Coleman, S. Howard, and L. Erofeeva (2002), A new tide model for the Antarctic ice shelves and seas, in *Ann Glaciol*, edited, pp. 247-254.

Payne, A. J., I.C. Rutt, A. Jenkins, and I. Joughin (2007), Numerical modeling of ocean-ice interactions under Pine Island Bay's ice shelf, *J Geophys Res-Oceans*, 112, C10019, doi:10.1029/2006JC003733.

Payne, A. J., A. Vieli, A. Shepherd, D.J. Wingham, and E. Rignot (2004), Recent dramatic thinning of largest West Antarctic ice stream triggered by oceans, *Geophys Res Lett*, 31, L23401.

Pedersen, F. B. (1980), Dense Bottom Currents In Rotating Ocean, *Journal Of The Hydraulics Division-Asce*, 106, 1291-1308.

Price, J. F., and M. O. Baringer (1994), Outflows And Deep-Water Production By Marginal Seas, *Progress In Oceanography*, 33, 161-200.

Rignot, E., and S. S. Jacobs (2002), Rapid bottom melting widespread near Antarctic ice sheet grounding lines, *Science*, 296, 2020-2023.

Rignot, E. (2008), Changes in West Antarctic ice stream dynamics observed with ALOS PALSAR data, *Geophys Res Lett*, 35, doi:10.1029/2008GL033365.

Rignot, E., and K. Steffen (2008), Channelized bottom melting and stability of floating ice shelves, *Geophys Res Lett*, 35, doi:10.1029/2007GL031765.

Schoof, C. (2007), Ice sheet grounding line dynamics: Steady states, stability, and hysteresis, *J Geophys Res-Earth*, 112, doi:10.1029/2006JF000664.

Shepherd, A., D.J. Wingham, and E. Rignot (2004), Warm ocean is eroding West Antarctic Ice Sheet, *Geophys Res Lett*, 31, L23402, doi:23410.21029/22004GL021106.

Thoma, M., A. Jenkins, D.M. Holland, and S. Jacobs (2008), Modelling Circumpolar Deep Water intrusions on the Amundsen Sea continental shelf, Antarctica, *Geophys Res Lett*, 35, doi:10.1029/2008GL034939.

Walker, R. T., T.K. Dupont, B.R. Parizek, and R. B. Alley (2008), Effects of basal-melting distribution on the retreat of ice-shelf grounding lines, *Geophys Res Lett*, 35, doi:17510.11029/12008GL034947.

Walker, R. T., and D. M. Holland (2007), A two-dimensional coupled model for ice shelf-ocean interaction, *Ocean Model*, 17, 123-139.

FIGURE CAPTIONS

Figure 1. Key barriers (numbered arrows) in the transfer of oceanic heat to an ice shelf may be spatially segregated. The barriers illustrated schematically here are: 1) the base of the open ocean mixed layer; 2) the ice shelf front; 3) the base of the sub-ice shelf mixed layer; 4) the ice shelf interface. Any unused heat may be advected out of the ice shelf cavity (dotted arrow). The black rectangle highlights the sub-ice shelf mixed layer subdomain, further described in figure 2.

Figure 2. In the reduced-gravity and 3-D numerical models used in these experiments, oceanic heat fluxes (where q_A , q_I , and q_E are advective, ice-ocean, and entrained heat fluxes, respectively) along the longitudinal axis of an ice shelf are discretized with a bulk mixed layer. The temperature of the mixed layer (T) is bounded by the in-situ freezing point (T_B) and the interior temperature (T_D).

Figure 3. Schematic a) plan and b) map views of the principal configuration (BASE) employed in these simulations. (a) depicts the ice shelf draft at $y=20$ km. Contours in (b) indicate the water column thickness (h_{WC}); the dotted line is the location of (a). Alternate ice shelf configurations (further described in table 1) are shown in (c-f). Vertical shading indicates the portion of the domain where interface heights, temperature, and salinity are restored to their initial conditions. Analysis of the simulations is performed only on the easternmost

3/5 of the model domain (hatched regions), limiting the influence of the applied restoring.

Figure 4. Steady-state mixed layer properties in the eastern 60 km of the BASE case ($T_D=1.0^\circ\text{C}$) are forced by strong spatial gradients in heat fluxes. In (a), the mixed layer temperature (T , $^\circ\text{C}$, shading) and in-situ freezing point (T_B , $^\circ\text{C}$, contours) are shown. The entrainment rate (e' , myr^{-1} , shading) and ice shelf melting rate (m' , myr^{-1} , contours) are shown in (b). (c) describes the mixed layer salinity (S , psu, shading), thickness (h , m, contours), and velocity (\mathbf{u} , ms^{-1} , vectors). In (d), meridionally integrated heat fluxes ($-Q_I$, the heat flux to the ice; Q_T , the entrained heat flux relative to the freezing point, and Q_E , the entrained heat flux) are plotted against the right hand axis. The excess heat flux (H_X) is overlain as a thick red line against the left hand axis. Vertical lines indicate the initiation (I), maintenance (M) and outflow (O) regions.

Figure 5. Mixed layer heat fluxes for alternate configurations indicate that distinct mixed layer regimes and inefficiency are pervasive features. In each panel, meridionally integrated heat fluxes ($-Q_I$, the heat flux to the ice; Q_T , the heat flux relative to the freezing point, and Q_E , the entrained heat flux) are plotted against the right hand axis. The excess heat (H_X) is overlain as a thick line against the left hand axis. The interior temperature (T_D) in each panel is 1.0°C .

Figure 6. Mixed layer heat fluxes exhibit different dependence on local slope, and their

sensitivity to slope is a function of the area over which quantities are averaged. Above, the values of γ_T (the ice-ocean transfer velocity), e' (the mixed layer entrainment rate), m' (the melting rate), and ΔT_I (the ice-mixed layer temperature gradient) are spatially averaged over the analysis region (“overall”, in solid symbols) and the first 5 km (“initiation”, in open symbols) for all configurations employed in these experiments ($T_D=1.0^\circ\text{C}$). The trendlines shown are for power laws of the form $x=c\theta^n$, where the exponent n is noted in the legend.

Figure 7. Melting rates are uniformly higher as interior temperature increases, but decreases in ice-ocean efficiency drive a departure of the area-averaged melting rates (\overline{m}_O' , myr^{-1}) from a quadratic dependence on thermal driving (ΔT_T^{MAX}) for all ice shelf configurations. A quadratic extrapolation of the BASE case melt rate based on the increase from $0-1^\circ\text{C}$ of thermal driving is included (black solid line) for comparison.

Figure 8. Area-integrated ice-ocean (circles) and entrained heat fluxes (triangles) diverge with increasing thermal driving in the BASE case. The difference between these two heat fluxes is approximately equal to the heat exported from the ice shelf cavity, shown with x's.

Figure 9. Regressions of e' and γ_T against (a) flow speed ($|u|$) and (b) $|u|\theta$ (e' only) indicates that entrained heat is strongly governed by basal slope. In both panels,

each grid point in the analysis region of the BASE simulation ($T_D=1.0^\circ\text{C}$) is plotted. In (a), γ shows only a slight departure from linearity with flow speed. Entrainment (e') is clearly a non-linear function of flow velocity; including slope (b) improves the regression dramatically, but e' remains systematically higher at high slopes.

Figure 10. The meridionally averaged a) excess heat (H_X) and b) ice-ocean temperature gradient (ΔT_I), shown for four interior temperatures ($0.0^\circ\text{C} < T_D < 1.5^\circ\text{C}$), reveals accumulation of heat not compensated by downstream cooling. Vertical lines separate the initiation (I), maintenance (M) and outflow (O) regions.

TABLES

Table 1. Details of alternate ice shelf configurations.¹

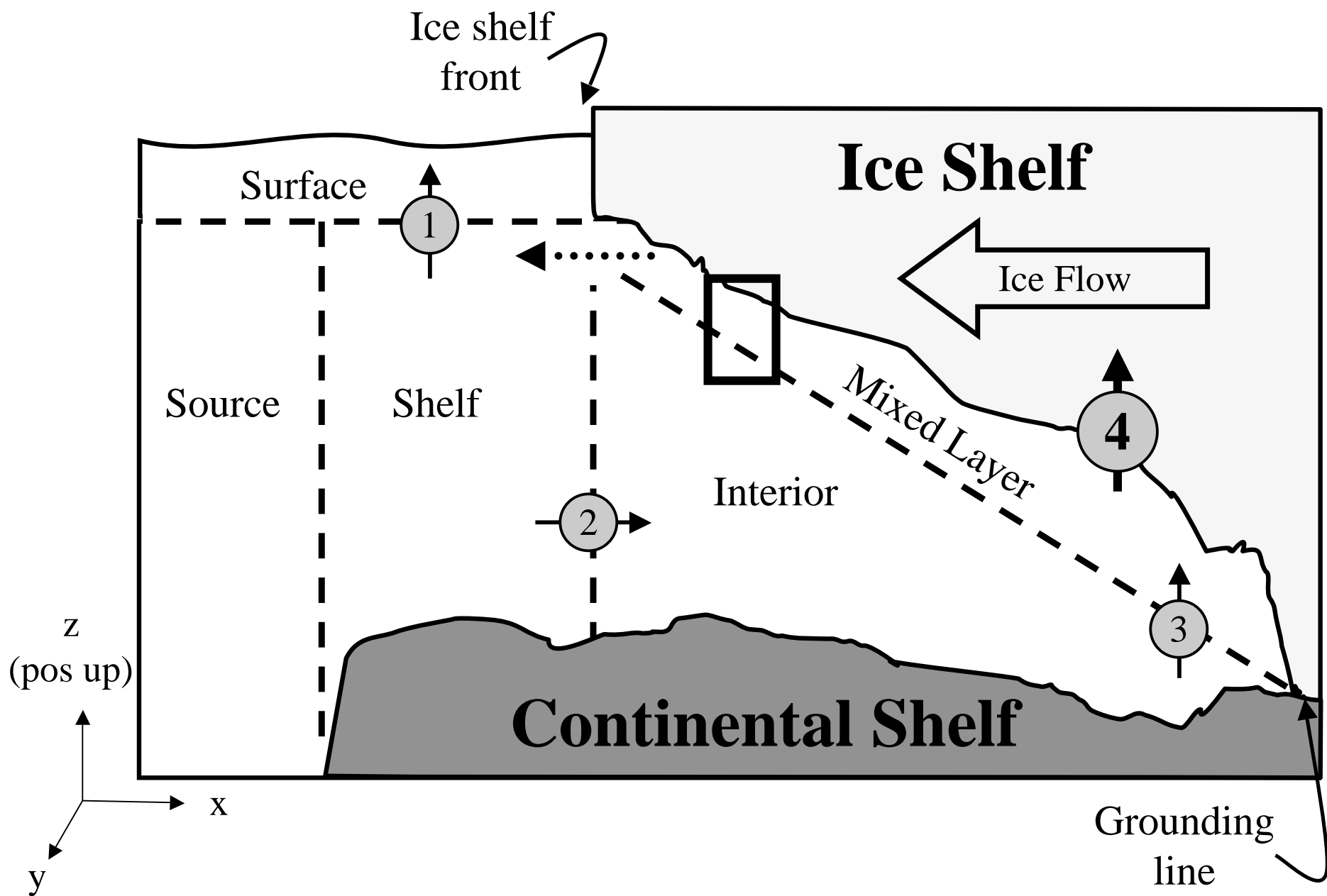
	W (km)	L (km)	A (10^3 km)	D (m)	$\theta_{max}(10^{-2})$	$\bar{\theta}_O(10^{-2})$	$\bar{\theta}_I(10^{-2})$
BASE	40	60	2.2	900	6.4	0.88	4.4
WIDE	80	60	4.4	900	6.4	0.88	4.4
LONG	40	120	4.6	900	6.4	0.42	4.4
DEEP	40	60	2.3	1200	8.6	1.21	5.9
BIG	80	120	8.7	900	3.2	0.44	2.9

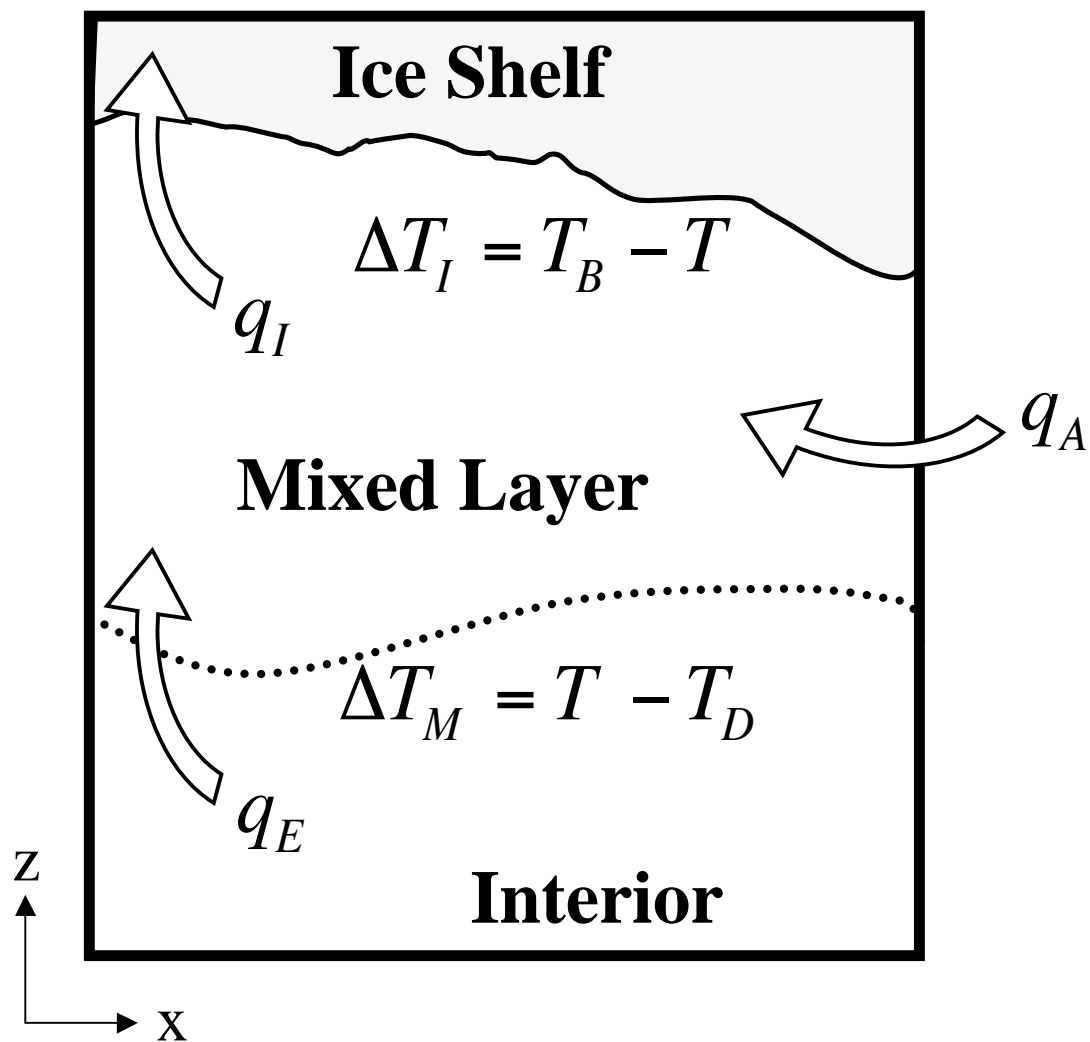
¹ W, L, and D are the maximum width, length, and depth of each ice shelf cavity. A is the area of the ice shelf base. The basal slope is averaged over the entire analysis region and the initiation (westernmost 5 km) region (O and I subscripts, respectively). All dimensions are for the analysis region of each simulation.

Table 2. Summary of temperature and shape sensitivity analysis.²

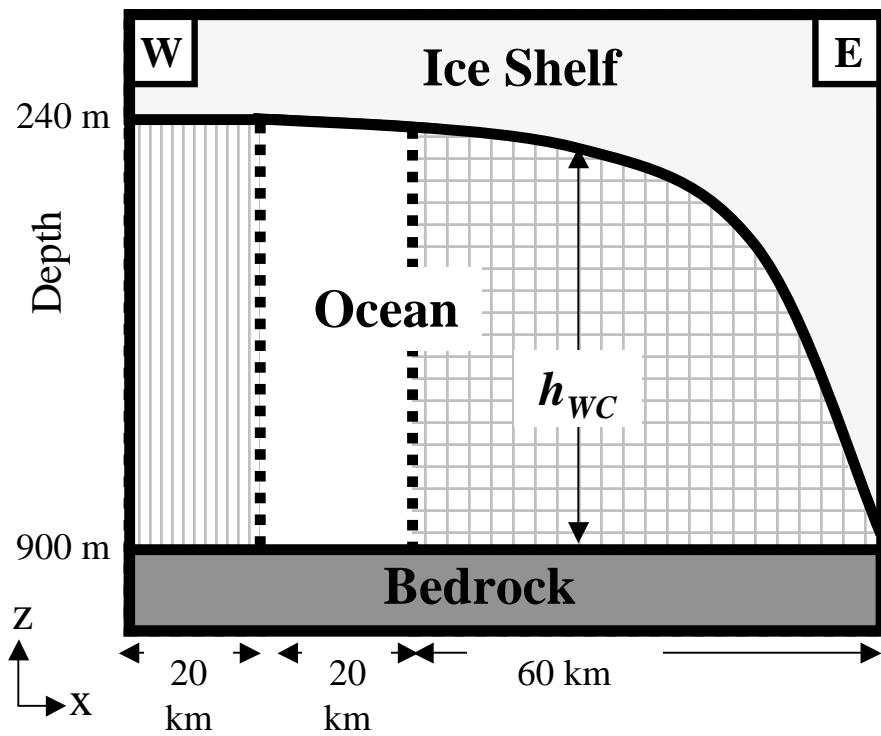
Simulation	\bar{m}'_O	\bar{m}'_I	\bar{m}'_{max}	$ x_{75\%} $	f_M	f_E
BASE						
-1.5	1.20	5.92	4.63	0.35	0.95	0.24
-0.5	5.49	19.87	15.30	0.44	0.90	0.25
0.5	11.90	38.45	29.61	0.47	0.89	0.26
1.5	21.03	60.29	46.61	0.54	0.87	0.24
WIDE						
-1.5	1.15	5.99	4.67	0.31	0.97	0.23
-0.5	5.43	19.95	15.38	0.42	0.94	0.25
0.5	11.95	38.42	29.71	0.46	0.92	0.26
1.5	20.40	60.49	46.95	0.50	0.91	0.29
LONG						
-1.5	0.65	6.76	5.49	0.18	0.92	0.27
-0.5	2.99	22.47	17.96	0.24	0.89	0.43
0.5	6.55	43.82	34.73	0.27	0.86	0.36
1.5	11.50	69.43	54.82	0.31	0.85	0.54
DEEP						
-1.5	2.31	10.02	7.84	0.36	1.01	0.39
-0.5	9.08	29.47	22.51	0.45	0.96	0.34
0.5	18.94	54.81	41.61	0.49	0.94	0.33
1.5	31.75	84.73	64.13	0.52	0.93	0.29
BIG						
-1.5	0.56	4.23	2.81	0.26	0.92	0.15
-0.5	2.58	13.77	8.92	0.33	0.86	0.22
0.5	5.92	26.39	17.00	0.40	0.85	0.26
1.5	10.94	41.56	26.47	0.52	0.84	0.30

² The melting rate (\bar{m}' , in myr^{-1}) is averaged over the entire analysis region and the initiation (westernmost 5 km) region (O and I subscripts, respectively). $|x_{75\%}|$ is the fraction of the analysis region over which 75% of the melting (integrated from the eastern boundary) occurs. For example, in the BASE, -1.5°C, simulation, 75% of basal melting occurs in the eastern 35% of the ice shelf.

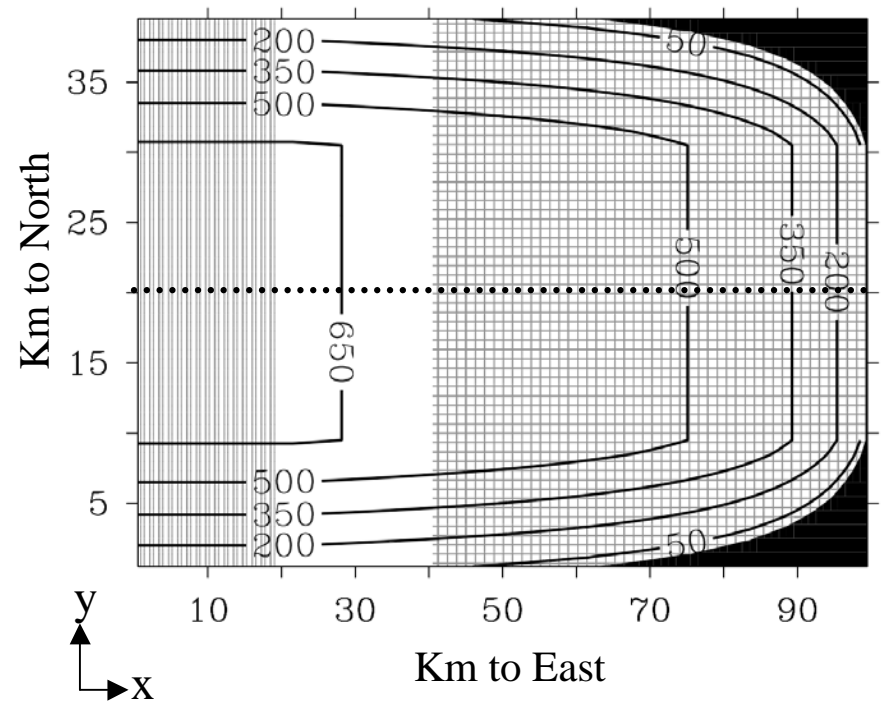




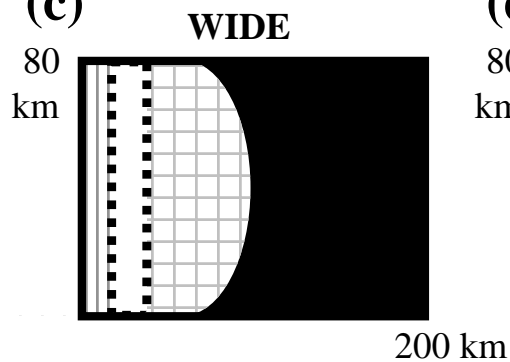
(a)



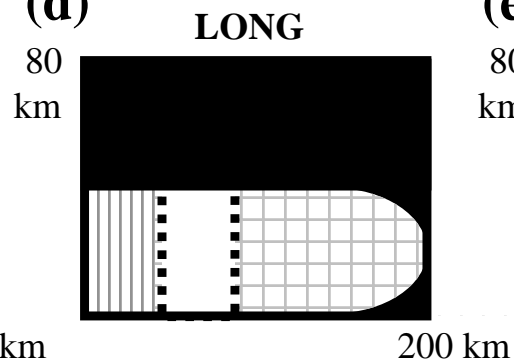
(b)



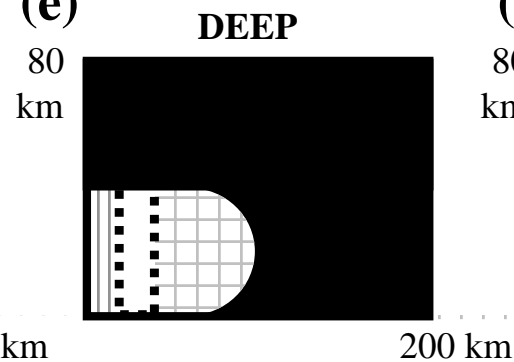
(c)



(d)



(e)



(f)

